polymers

MDPI

Article

Thermal Energy Storage and Mechanical Performance of Foamed Concrete Incorporating Volcanic Rock/Paraffin Shape-Stabilized Phase Change Materials

Hai Yu *, Changgeng Liu * and Rufeng Ma

School of Hydraulic Engineering and Smart Cities, North Minzu University, Yinchuan 750021, China; marufeng0220@126.com

* Correspondence: yuhai1212@126.com (H.Y.); 18769769610@163.com (C.L.)

Abstract

To investigate the effects of volcanic rock/paraffin shape-stabilized PCM (SS-PCM) incorporation on the thermal energy storage and mechanical performance of foamed concrete (FC). Porous volcanic rock was used as the supporting matrix, and a volcanic rock–paraffin shape-stabilized phase change material (SS-PCM) was prepared by vacuum adsorption of molten paraffin. The resulting composite phase change material was then incorporated into foamed concrete at different volume fractions, followed by temperature-response, compressive-strength, energy-absorption, and damage-evolution tests and analyses to evaluate its feasibility for engineering applications. The experimental results showed that, after 60 min of heating, the specimens incorporating SS-PCM particles with sizes of 0.5, 1.0, and 2.0 mm exhibited maximum temperature differences of 3.9, 4.3, and 1.6 °C, respectively, compared with the control group without SS-PCM, corresponding to percentage differences of 8.3%, 9.1%, and 3.4%, respectively. The compressive strength test results indicated that the incorporation of SS-PCM resulted in compressive strength reductions ranging from 4.2% to 43.0%. Among these, the maximum compressive strength reduction of 43.0% was observed in the specimen containing 30% SS-PCM with a particle size of 1 mm at an ambient temperature of 75 °C, corresponding to a decrease of 4.43 MPa compared with the control group without SS-PCM at the same temperature. Furthermore, digital image correlation (DIC) analysis indicated that the ambient temperature played an important role in the damage evolution mode of the SS-PCM-containing specimens. As the ambient temperature increased, strain localization progressively evolved from a single dominant path to a more complex damage pattern characterized by multipath propagation, branching, and coalescence.

Keywords: shape-stabilized phase change materials; foamed concrete; volcanic rock; thermal regulation performance; damage evolution

Academic Editor: Stefano Vecchio Ciprioti

Received: 26 October 2026
Revised: 13 November 2026
Accepted: 24 November 2026
Published: 26 November 2026

Copyright: © 2026 by the authors. Licensee MDPI, Basel, Switzerland. This article is an open access article distributed under the terms and conditions of the Creative Commons Attribution (CC BY) license.

1. Introduction

The continuous increase in building operational energy consumption has made the passive thermal regulation capability of building envelopes a key research focus in the development of low-energy building materials. Phase change material (PCM) can absorb thermal energy during melting and release it upon solidification while maintaining a relatively stable temperature plateau within a narrow temperature range, and is therefore

considered an effective approach for enhancing the thermal buffering capacity of building envelopes while reducing heating and cooling demand [1–4]. In recent years, phase change materials (PCMs) have been increasingly incorporated into building envelope systems, with their applications extending to walls, roofs, floors, and composite envelope assemblies. With increasing attention to building energy efficiency, envelope materials are now required to provide more than structural support, with thermal regulation and energy storage becoming increasingly important functions [5,6].

Foam concrete is characterized by its lightweight nature and low thermal conductivity due to its highly porous internal structure, making it widely used in building walls, roof insulation layers, infill structures, and prefabricated components [7,8]. Its low density and excellent thermal and acoustic insulation properties make it an important material for energy-efficient buildings. However, its complex pore structure also introduces uncertainties in its performance, as its mechanical properties and heat transfer behavior are jointly influenced by pore structure, density, and service conditions [9,10]. Extensive research has been conducted worldwide to optimize the performance of foam concrete. Beskopylny et al. [11] investigated the effects of polystyrene particles on the mechanical and thermal conductivity properties of lightweight concrete by combining finite element simulations with experimental investigations, enabling effective prediction of the material properties. Yildizel et al. [12] incorporated waste tire steel fibers and rubber particles into foam concrete and optimized the mix proportions using the Taguchi method and artificial neural networks. Their results indicated that the incorporation of steel fibers could mitigate the adverse effects of rubber particles on the mechanical properties of the material. Mydin et al. [13] prepared foamed mortar by partially replacing natural sand with recycled polyethylene terephthalate (PET) particles. Their findings demonstrated that an appropriate PET content could improve the thermal insulation performance and durability of the material, whereas excessive PET incorporation could lead to a reduction in mechanical properties. Furthermore, fiber reinforcement, mineral admixtures, and lightweight aggregate modification have also been employed to improve the toughness, pore structure, and durability of foam concrete [14,15]. The aforementioned studies demonstrate that the incorporation of various functional components and the optimization of material composition can improve the overall performance of foam concrete to some extent. However, further enhancing its thermal performance while maintaining adequate mechanical load-bearing capacity remains a key challenge in the development of this material.

Previous studies have investigated the effects of phase change materials (PCMs) on the thermal and mechanical properties of various materials. Yang et al. [16] incorporated microencapsulated PCMs into an alkali-activated binder made from slag and fly ash, then investigated the changes in its mechanical properties and heat-storage performance. Relative to the C0 reference, the time required for C5, C10, C20, S5, and S10 to reach 40 °C increased by 24.5%, 71.4%, 167.3%, 38.8%, and 100%, respectively, indicating a clear delay in temperature rise after PCM incorporation. This thermal benefit was accompanied by a substantial loss in strength. The compressive strength decreased by 69.8% at 3 d and by 70.7% at 7 d. Zheng et al. [17] developed a microencapsulated phase change material and evaluated its temperature-regulation performance. The material showed good thermal control, lowering the peak temperature by 13.98 °C under daytime outdoor conditions and by 2.84 °C in laboratory tests. Kocyigit et al. [18] developed a shape-stabilized phase change material using basalt powder and capric acid and evaluated its mechanical and thermal properties. After 500 melting–solidification cycles, the material retained 99.5% of its initial heat-storage capacity and continued to effectively reduce temperature fluctuations. Fu et al. [19] prepared a $CaCl_2$-based aerogel phase change material and incorporated it into foamed concrete blocks. The modified blocks underwent phase transition at around 27.2 °C, along with noticeable increases in heat value, specific heat capacity, and

thermal conductivity. The ability to store large amounts of thermal energy and regulate temperature effectively, and favorable thermal cycling stability of PCMs have led to their increasingly widespread application in building materials and engineering.

Among various phase change materials (PCMs), paraffin-based organic phase change materials are widely adopted in building and room-temperature thermal storage systems owing to their superior properties including high latent heat of phase change, favorable chemical stability, low corrosivity, limited supercooling degree, and tunable phase transition temperature [20]. However, paraffin has an intrinsically low thermal conductivity, and its direct incorporation into cement-based materials may disrupt matrix continuity and weaken interfacial bonding [21,22]. Therefore, maintaining the thermal energy storage capacity of PCMs while improving their shape stability and engineering applicability remains a key challenge in the development of PCM-integrated building materials [23,24].

Shape-stabilized phase change materials (SS-PCMs) offer a feasible solution to address the aforementioned challenges. These materials typically employ porous supports, such as expanded graphite, expanded perlite, diatomite, and lightweight porous aggregates, to retain PCMs within their pore structures through capillary adsorption, surface tension, and pore confinement, thereby reducing the migration and leakage of liquid PCMs during phase transitions [25,26]. Porous supports such as diatomite, expanded perlite, and recycled porous aggregates have been widely used in the preparation of SS-PCMs, exhibiting favorable PCM adsorption capacity and thermal cycling stability [27–29]. Volcanic rock, as a natural porous material, is characterized by a well-developed pore structure, low density, and abundant availability, and can also immobilize phase change materials within its pores through adsorption. However, a systematic understanding of the thermal energy storage and temperature regulation performance, mechanical response, and damage evolution behavior of foam concrete incorporating volcanic rock-supported PCMs remains limited. In particular, the effects of carrier particle size, incorporation ratio, and ambient temperature on the overall performance of the material require further investigation.

In this study, porous volcanic rock particles were used as supports to prepare a shape-stabilized phase change material (SS-PCM) through vacuum impregnation with paraffin, which was subsequently incorporated into foam concrete. The effects of SS-PCM particle size, incorporation ratio, and ambient temperature on the thermal response, mechanical properties, and damage evolution of foam concrete were systematically investigated. Furthermore, digital image correlation (DIC) was employed to characterize the deformation behavior and failure process of the specimens under loading, thereby elucidating the deformation and damage evolution mechanisms under different influencing factors. This study provides a theoretical basis for the development of novel building materials integrating lightweight characteristics, thermal insulation, and thermal energy storage capabilities [30].

2. Materials and Experimental Methods

2.1. Raw Materials and Specimen Preparation

Ordinary Portland cement (P·O 42.5) produced by Ningxia Saima Cement Co., Ltd. (Yinchuan, Ningxia, China) was used, with a minimum 28-day compressive strength of 42.5 MPa. Table 1 summarizes the main performance parameters of the material. Paraffin was purchased from Shengbang Plastic Trading Co., Ltd. (Dongguan, Guangdong, China), and volcanic rock particles were obtained from Tengchong, Yunnan Province, China. The surface morphology of the volcanic rock particles is shown in Figure 1. A commercially available animal-protein foaming agent supplied by Risheng Nissho Chemical (Zhengzhou, Henan, China) was used, and laboratory water was used as the mixing water.

https://doi.org/10.3390/polym18232982

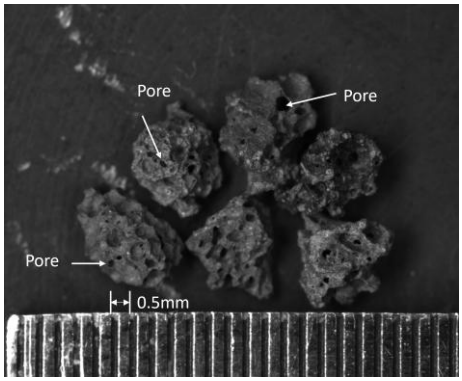


Figure 1. Surface morphology of volcanic rock particles.

The specimen preparation consisted of two stages: preparation of the shape-stabilized phase change material (SS-PCM) and fabrication of the SS-PCM foamed concrete specimens. The preparation procedure of the SS-PCM was as follows. First, the volcanic rock particles were pretreated by thoroughly washing them with clean water. Subsequently, the material was oven-dried at 60 °C for 24 h to remove residual moisture. Paraffin was first heated until fully melted and mixed with the dried volcanic rock particles under continuous stirring. The resulting mixture was placed in a vacuum chamber and subjected to vacuum impregnation at a pressure of −0.08 MPa and a temperature of 50 °C for 8 h. A paraffin-to-volcanic rock particle mass ratio of 1.5:1 was maintained to ensure sufficient paraffin infiltration into the pores of the volcanic rock particles. Continuous heating was applied throughout the impregnation process to prevent paraffin solidification, which could otherwise reduce the impregnation efficiency. After impregnation, the mixture was removed from the vacuum chamber, and excess free paraffin on the particle surfaces was removed using filter paper to obtain the shape-stabilized phase change material (SS-PCM).

The basic properties of SS-PCM are presented in Table 2. The adsorption rate of volcanic rock particles gradually increased with increasing particle size, with the lowest adsorption rate observed for the 0.5 mm particles, followed by the 1.0 mm particles, while the 2.0 mm particles exhibited the highest adsorption rate. The paraffin loading was determined by subtracting the mass of the volcanic rock particles before impregnation from their mass after impregnation and removal of excess free paraffin from the particle surfaces. The observed particle size dependence of paraffin loading may be associated with differences in the accessible pore volume and pore network integrity among volcanic rock particles of different sizes. Smaller particles may lose part of their original internal pore structure during crushing and sieving, resulting in a relative reduction in the effective pore space available for paraffin impregnation. In contrast, larger particles may retain more intact and interconnected internal pores, providing favorable conditions for the infiltration and retention of molten paraffin within the particles under vacuum conditions. Furthermore, differences in pore-throat structure and pore connectivity may also influence the infiltration efficiency and final paraffin loading during the vacuum impregnation process. Therefore, the higher paraffin adsorption rate exhibited by larger volcanic rock particles under vacuum conditions may be attributed to the combined effects of accessible pore volume, pore structural characteristics, and the vacuum impregnation process.

The SS-PCM foamed concrete was prepared as follows. First, cement and mixing water were combined at a water-to-cement ratio of 0.5 and mixed for 2 min to obtain a homogeneous cement paste. The animal-protein foaming agent was mixed with water in a mass ratio of 1:40, and the mixture was passed through a foam generator to obtain a stable foam. The prepared foam was gradually incorporated into the cement paste, and the foam dosage was adjusted until the density of the paste reached the target value of 1200 kg/m^3.

The pre-prepared SS-PCM was then added, followed by continued mixing until it was uniformly dispersed throughout the paste. Finally, the mixed slurry was cast into molds and compacted by vibration. After 24 h, the specimens were demolded and subsequently cured in a standard curing chamber for 28 days at a temperature of (20 ± 2) °C and a relative humidity of not less than 95%. The preparation procedure of the SS-PCM foamed concrete is illustrated in Figure 2.

Table 1. Basic Parameters of Cement.

Cement	Specific Surface Area/($m^2 \cdot kg^{-1}$)	Setting Time/min		Bend Strength/MPa		Compression Strength/MPa	
		Initial Setting	Final Setting	3 d	28 d	3 d	28 d
P·O 42.5	340	60	300	5.5	9.5	30.1	50.4

Table 2. Basic properties of SS-PCM.

Group	Bulk Density/$g \cdot cm^{-3}$	Adsorption Rate/%
0.5 mm	0.823	12%
1.0 mm	0.794	17%
2.0 mm	0.778	25%

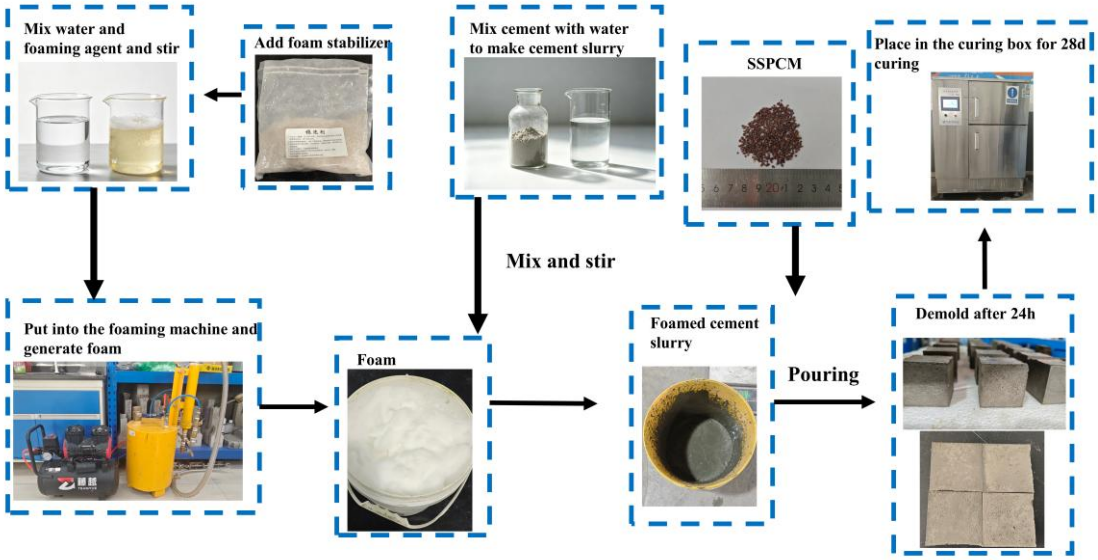


Figure 2. Preparation procedure of SS-PCM foamed concrete specimens.

2.2. Experiment Design

A total of 30 groups were included in the compressive strength test, with three replicate specimens prepared for each group. Considering the pore structure of foamed concrete, matrix strength, and SS-PCM particle size, as well as the loading range and measurement accuracy of the testing machine, cubic specimens measuring 40 × 40 × 40 mm were employed for the compression tests. Considering that phase change energy storage materials are commonly employed as thin thermal-regulation layers within walls, floors, or suspended ceilings in building envelope systems, plate specimens measuring 70 × 70 × 20 mm were used for the temperature-response tests to better represent the geometric characteristics of practical engineering applications.

The ambient temperatures for the compression tests were selected according to the phase-change behavior of paraffin and the differences in material properties among its various phase states. The paraffin used in this study has a phase-transition temperature of approximately 25 °C. Accordingly, ambient temperatures of −25, 25, and 75 °C were adopted to represent conditions in the solid state, near the phase-transition range, and in the liquid state, respectively. These temperatures therefore capture the thermal conditions before, during, and after the phase change. These temperature conditions allow the compressive behavior and damage development of SS-PCM foamed concrete to be compared across different temperatures and phase states. They also help clarify how its mechanical response changes with ambient temperature.

Based on the aforementioned experimental conditions, SS-PCM particle size, volumetric incorporation ratio, and ambient temperature were selected as experimental variables to investigate their effects on the mechanical properties of foam concrete. The SS-PCM particles were prepared by vacuum impregnation of molten paraffin into volcanic rock particles with diameters of 0.5, 1.0, and 2.0 mm, respectively. The target density of the reference foamed cement paste without SS-PCM was set at 1200 kg/m^3. On this basis, SS-PCM particles were incorporated using an equal-volume replacement method at volumetric incorporation ratios of 10%, 20%, and 30%. Specifically, the corresponding volumes of SS-PCM particles were used to replace equal volumes of the foamed cement paste. The calculation is expressed by Equation (1). The density of 1200 kg/m^3 represents the target design density of the reference foamed cement paste before SS-PCM incorporation. After the incorporation of SS-PCM, no additional adjustments were made to the paste composition or the quantities of other constituent materials to control the final density of the composite. The measured dry densities of the resulting specimens are presented in Table 3. The specimens were designated using the format "volumetric incorporation ratio/particle size–temperature", and the detailed specimen combinations are presented in Table 4.

$$\varphi_{SS-PCM} = \frac{V_{SS-PCM}}{V_{SS-PCM} + V_{\text{paste}}} \times 100\% \quad (1)$$

$\varphi_{SS\text{-}PCM}$: Volumetric incorporation ratio of SS-PCM (%);

$V_{SS\text{-}PCM}$: Volume of SS-PCM composite particles, including the volcanic rock framework and the paraffin impregnated within its pores;

V_{paste}: Volume of foamed cement paste in the composite.

Table 3. Dry densities of foam concrete specimens.

Group		Density (kg/m^3)		
0%	SS-PCM	10 vol%	20 vol%	30 vol%
1071	0.5 mm	1124	1114	1152
1071	1.0 mm	1101	1132	1184
1071	2.0 mm	1132	1118	1119

Table 4. Summary of specimen designations for volcanic rock–paraffin shape-stabilized phase change foamed concrete.

Compression/Temperature Test Specimen		
0 vol% SS-PCM/FC-−25	0 vol% SS-PCM/FC-25	0 vol% SS-PCM/FC-75
10 vol% SS-PCM (0.5 mm)/FC-−25	10 vol% SS-PCM (0.5 mm)/FC-25	10 vol% SS-PCM (0.5 mm)/FC-75
10 vol% SS-PCM (1.0 mm)/FC-−25	10 vol% SS-PCM (1.0 mm)/FC-25	10 vol% SS-PCM (1.0 mm)/FC-75
10 vol% SS-PCM (2.0 mm)/FC-−25	10 vol% SS-PCM (2.0 mm)/FC-25	10 vol% SS-PCM (2.0 mm)/FC-75
20 vol% SS-PCM (0.5 mm)/FC-−25	20 vol% SS-PCM (0.5 mm)/FC-25	20 vol% SS-PCM (0.5 mm)/FC-75
20 vol% SS-PCM (1.0 mm)/FC-−25	20 vol% SS-PCM (1.0 mm)/FC-25	20 vol% SS-PCM (1.0 mm)/FC-75
20 vol% SS-PCM (2.0 mm)/FC-−25	20 vol% SS-PCM (2.0 mm)/FC-25	20 vol% SS-PCM (2.0 mm)/FC-75
30 vol% SS-PCM (0.5 mm)/FC-−25	30 vol% SS-PCM (0.5 mm)/FC-25	30 vol% SS-PCM (0.5 mm)/FC-75
30 vol% SS-PCM (1.0 mm)/FC-−25	30 vol% SS-PCM (1.0 mm)/FC-25	30 vol% SS-PCM (1.0 mm)/FC-75
30 vol% SS-PCM (2.0 mm)/FC-−25	30 vol% SS-PCM (2.0 mm)/FC-25	30 vol% SS-PCM (2.0 mm)/FC-75

2.3. Experimental Characterization

2.3.1. Microstructural Analysis (SEM)

The microstructure and interfacial characteristics of SS-PCM foam concrete were examined using scanning electron microscopy (SEM, ZEISS, Oberkochen, Germany). First, representative small samples were collected from the interior of specimens cured to the specified age and dried to remove free water. Subsequently, freshly fractured surfaces were selected for observation. The samples were mounted on SEM stubs using conductive adhesive and sputter-coated with gold to improve their electrical conductivity and imaging quality. Finally, scanning electron microscopy was performed at different magnifications to examine the pore morphology, cement hydration products, and interfacial bonding between the SS-PCM particles and the cementitious matrix, thereby analyzing the effects of SS-PCM particle size on the microstructure of foam concrete.

2.3.2. DSC Test

Differential scanning calorimetry (DSC) was used to examine the phase-change behavior of paraffin and SS-PCM with a Q2000 calorimeter (TA Instruments, New Castle, DE, USA). A 10 mg sample was sealed in an aluminum crucible and tested under high-purity nitrogen flowing at 50 mL/min. The sample was heated from −10 to 50 °C at a heating rate of 5 °C/min and held at 50 °C for 10 min. It was then cooled to −10 °C at the same rate, while the heat-flow signals were recorded throughout the heating and cooling processes. The phase transition temperatures of the samples, including the onset and peak temperatures, were determined from the positions of the melting endothermic and solidification exothermic peaks in the DSC curves. After baseline correction of the DSC curves, the latent heat of phase transition was calculated according to Equation (2) proposed by He et al. [31].

$$Q_{\mathrm{pc}} = \int_{t_1}^{t_2} \left(\frac{\delta Q}{dt}\right)_{pc} dt \tag{2}$$

2.3.3. TGA Test

Thermogravimetric analysis (TGA) was employed to characterize the thermal decomposition behavior and thermal stability of the SS-PCM using a TGA Q5000 thermogravimetric analyzer (TA Instruments, New Castle, DE, USA). Before testing, the specimens were thoroughly dried and ground into a uniform powder. Approximately 10 mg of the powder was then placed in an aluminum crucible. The test was performed under high-purity nitrogen flowing at 30 mL/min to minimize oxidation of the sample during

heating. A heating ramp of 10 °C/min was applied to raise the temperature from room temperature to 800 °C, while its mass was continuously recorded as a function of temperature and time.

TG curves were used to track changes in specimen mass during heating and to characterize the associated thermal decomposition behavior. The curves provide information on mass loss, the onset of decomposition, the temperature corresponding to the maximum decomposition rate, and the residual mass at elevated temperatures. These parameters were used to assess the thermal stability of the composite and the decomposition behavior of its individual components.

2.3.4. Temperature-Response Test

Temperature response tests were conducted on specimens cured for 28 days. Figure 3 illustrates the schematic diagram of the temperature response testing setup, which mainly consisted of a constant-temperature heating plate (BYA, Dongguan, Guangdong, China), thermocouples (Teans, Jiangsu, China; measurement accuracy: 0.1 °C), and a computer. During the experiment, a constant-temperature heating plate was used to heat the specimens from one side to evaluate their temperature response characteristics under continuous thermal exposure following the incorporation of SS-PCM. The temperature was uniform across the entire surface of the heating plate. The heating plate temperature was set to 50 °C, and specimens measuring 70 mm × 70 mm × 20 mm were placed directly on the heating plate with their bottom surfaces in contact with the plate. No additional thermally conductive or insulating materials were placed between the specimens and the heating plate, allowing heat to be transferred into the specimens primarily through contact conduction at the bottom surface, while their lateral surfaces remained directly exposed to the ambient air. A temperature measurement point was positioned at the center of the top surface of each specimen, and the surface temperature was recorded at 1 min intervals to characterize the temperature response during heat transfer from the bottom to the top of the specimen. After 90 min of continuous heating, the heating plate was switched off, and the specimens were allowed to cool naturally while remaining on the heating plate in a constant-temperature environment of 15 °C. Temperature data were continuously recorded until 250 min. The temperature data recorded at 60 min were used to compare the temperature response characteristics of specimens incorporating SS-PCM particles with different particle sizes and volumetric incorporation ratios.

In the experiment, 50 °C was the set temperature of the heating plate. Although the bottom surface of the specimen was in direct contact with the heating plate, a certain degree of thermal contact resistance still existed at the interface. Meanwhile, convective and radiative heat exchange between the top and lateral surfaces of the specimen and the surrounding environment resulted in some heat loss. Therefore, this experiment was primarily designed to compare the relative temperature response characteristics of specimens incorporating different SS-PCM particles under identical experimental conditions. Furthermore, after the heating plate was switched off, its residual heat and gradual cooling may have continued to influence heat transfer between the plate and the specimens. Therefore, the measured cooling curves reflect the combined thermal response of the specimens and the heating plate rather than the independent cooling behavior of the specimens.



Figure 3. Schematic diagram of the temperature-response test setup.

2.3.5. Compressive Strength Test

Compression tests were conducted using an electronic universal testing machine (MTS Systems Corporation, Eden Prairie, MN, USA) under displacement-controlled loading at a rate of 2 mm/min.

Prior to testing, the specimens were naturally dried at room temperature until a constant mass was achieved. Subsequently, the specimens were placed in a constant-temperature chamber for 12 h to allow their temperatures to reach the designated values and stabilize. After temperature conditioning, the specimens were removed from the chamber and subjected to compression tests at room temperature. During compressive loading, the experimental data were continuously recorded using a data acquisition system, while the deformation process of the specimens was captured using a dual-CCD camera system (China Daheng Group, Inc., Beijing, China) with an image resolution of 3088 × 2064 pixels and an acquisition frequency of 10 Hz. Subsequently, the acquired images were analyzed using the open-source digital image correlation (DIC) software Ncorr (version 1.2.2, Georgia Institute of Technology, Atlanta, GA, USA) developed by Blaber et al. [32] to obtain the full-field displacement and strain distributions of the specimens. The strain fields were calculated using the Green–Lagrangian strain tensor, with local displacement gradients determined by the least-squares fitting method. The DIC results were primarily used to characterize the spatial distribution of strain localization and the evolution of damage in the specimens during compressive loading.

3. Results and Discussion

3.1. Performance Analysis of SS-PCM

3.1.1. Scanning Electron Microscopy (SEM) Analysis and Leakage Testing

Figure 4 presents the SEM images of SS-PCM foam concrete specimens at different magnifications. As shown in Figure 4 a,b, numerous pores of varying sizes are distributed throughout the specimens, some of which exhibit approximately spherical shapes. In certain regions, the pores are densely distributed, resulting in relatively thin cementitious matrix walls between adjacent pores and thereby reducing the continuity of the internal load-bearing structure. At higher magnification, as shown in Figure 4c, microcracks and structural discontinuities can be observed in the local pore walls and on the surface of the cementitious matrix, indicating the presence of microstructural defects within the specimen. Further examination of Figure 4d reveals irregular cavities in certain regions, which may have formed as a result of volcanic rock particles being pulled out of the cementitious matrix during compressive failure, suggesting relatively weak interfacial bonding between the SS-PCM particles and the cementitious matrix. This may be associated with the formation of an interfacial transition zone (ITZ) between the particles and the cementitious matrix. Due to differences in surface morphology, stiffness, and deformation characteristics between the two phases, local structural heterogeneity and stress concentration may occur within the ITZ. Under external compressive loading, microcracks tend to

initiate near the interfaces and propagate along them, potentially leading to debonding and pull-out of the particles from the cementitious matrix, thereby weakening the stress transfer capacity. Meanwhile, the incorporation of SS-PCM particles may disrupt the continuity of the original load-bearing framework of the cementitious matrix, altering local load transfer paths. Therefore, the reduction in the compressive strength of SS-PCM foam concrete may be primarily attributed to insufficient interfacial bonding between the particles and the cementitious matrix, localized weaknesses in the interfacial transition zone, and disruption of the continuity of the load-bearing framework of the cementitious matrix.

Li and Liu [33] evaluated the leakage resistance of composite phase change materials using a filter paper leakage test by observing the wetting traces on the filter paper after heating the samples at 60 °C. Based on the same testing principle, pure paraffin and SS-PCM particles with different particle sizes were subjected to isothermal heating at 50 °C for 1 h to evaluate their shape stability and leakage resistance. The results are shown in Figure 5. Before heating, both pure paraffin and SS-PCM particles of different sizes retained their initial shapes. After isothermal heating, pure paraffin melted significantly and formed a large wetted area on the filter paper, indicating its susceptibility to flow and leakage in the molten state. In contrast, SS-PCM particles with sizes of 0.5, 1.0, and 2.0 mm exhibited no large-scale wetting comparable to that of pure paraffin, with only slight wetting traces observed in localized areas, indicating that the porous volcanic rock framework could suppress the migration and leakage of molten paraffin to some extent. This may be attributed to the pore structure and capillary forces within the volcanic rock, which help retain molten paraffin. Overall, the SS-PCM particles exhibited good macroscopic leakage resistance under the test conditions of 50 °C for 1 h, providing preliminary experimental evidence supporting their potential application in foam concrete.

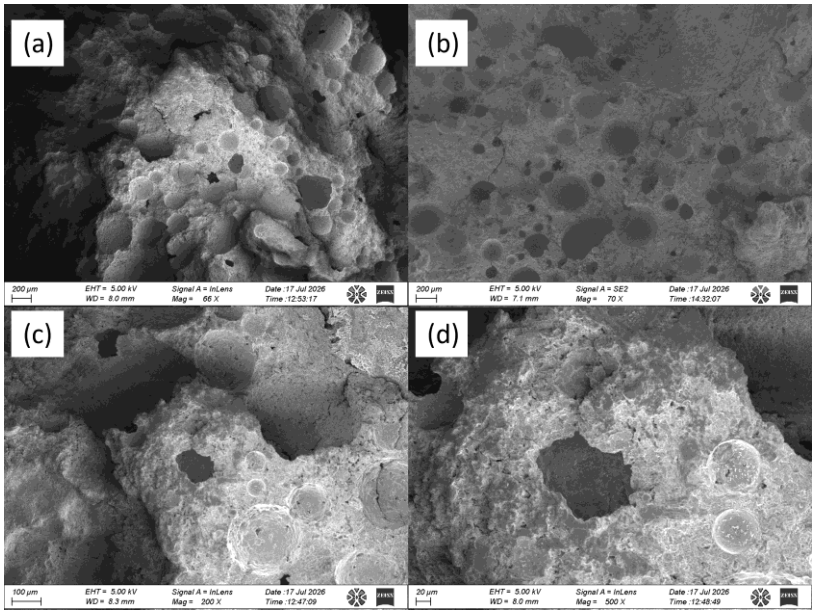


Figure 4. SEM micrographs of fractured SS-PCM foam concrete at different magnifications: (**a**) 65×, (**b**) 70×, (**c**) 200×, and (**d**) 500×.

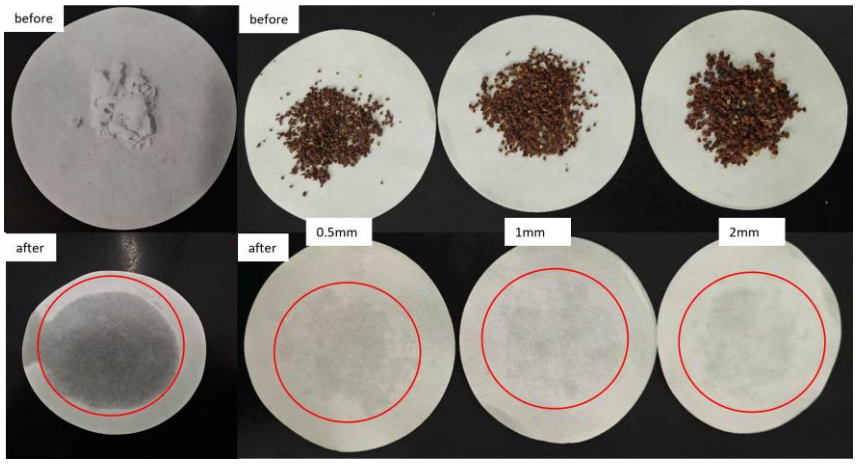


Figure 5. Leakage test results of pure paraffin and SS-PCM particles before and after heating.

3.1.2. DSC Thermal Analysis

Figure 6 presents the differential scanning calorimetry (DSC) curves of pure paraffin and SS-PCM particles during a complete heating–cooling cycle. As shown in Figure 6, both pure paraffin and SS-PCM exhibit a single endothermic peak during heating and a single exothermic peak during cooling, indicating that the prepared SS-PCM particles retain their solid–liquid phase transition characteristics. Compared with the melting peak temperature of pure paraffin (26.05 °C), the SS-PCM particles with diameters of 0.5, 1.0, and 2.0 mm exhibit melting peak temperatures of 24.82, 24.56, and 25.61 °C, respectively, indicating varying degrees of temperature shift. Previous studies have demonstrated that the spatial confinement effect and pore-wall interfacial interactions in porous media can influence the molecular arrangement and crystal growth behavior of paraffin, thereby altering its melting characteristics [34,35]. Furthermore, the volcanic rock framework and the paraffin confined within its pores form a heterogeneous heat transfer system. The pore structure and thermal resistance at the solid–liquid interface may affect heat transfer and local temperature distribution, thereby influencing the apparent phase transition peak temperature measured by DSC [36]. Therefore, the observed shifts in the melting peak temperatures of SS-PCM may be associated with the combined effects of pore confinement, interfacial interactions, and heat-transfer processes, as suggested by previous studies [34–36].

On the other hand, the phase change enthalpy of SS-PCM exhibits a pronounced particle size dependence. As shown in Table 5, the phase change enthalpy was determined based on the total mass of SS-PCM, including the volcanic rock framework and the paraffin absorbed within its pores. As the particle size increased from 0.5 mm to 1 and 2 mm, the melting latent heat increased from 14.09 $J \cdot g^{-1}$ to 21.31 and 34.74 $J \cdot g^{-1}$, respectively, while the solidification latent heat increased from 14.01 $J \cdot g^{-1}$ to 20.77 and 32.85 $J \cdot g^{-1}$, respectively. Since the volcanic rock framework itself does not contribute to the latent heat of phase transition, the thermal energy storage capacity of the composite primarily depends on the effective paraffin loading and the extent of its phase transition. The infiltration of paraffin into the porous framework is mainly governed by capillary forces, pore connectivity, and pore-throat structure. Differences in pore network integrity and available pore space among particles of different sizes consequently affect the actual paraffin loading. Meanwhile, the confinement effect imposed by the pore walls inhibits the crystallization of a portion of the paraffin, preventing it from fully participating in the phase transition [34,35]. As the particle size increases, larger particles retain more accessible pore space for paraffin infiltration, thereby increasing the paraffin loading. Meanwhile, a greater proportion of the paraffin within larger particles is subjected to weaker pore-wall confinement, which

facilitates the ordered arrangement of paraffin molecules and crystal growth, thereby increasing the extent of effective phase transition. Therefore, the combined increase in effective paraffin loading and the extent of phase transition may be the primary reason for the higher latent heat exhibited by SS-PCM particles with larger particle sizes.

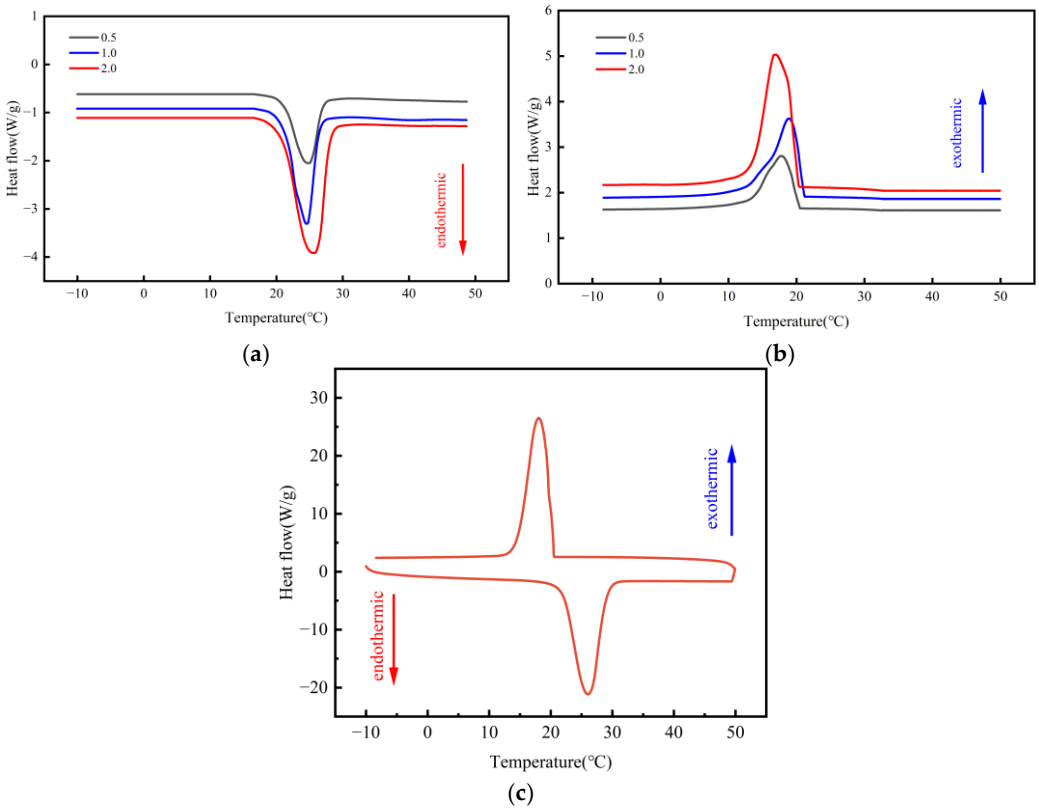


Figure 6. DSC curves of the samples: (**a**) SS-PCM during heating; (**b**) SS-PCM during cooling; (**c**) paraffin.

Table 5. Phase-change parameters of SS-PCMs.

Sample	Melting		Cooling	
	T_m (°C)	ΔH_m (J·g^{-1})	T_c (°C)	ΔH_c (J·g^{-1})
Paraffin	26.05	166	18.03	150
SS-PCM-0.5	24.82	14.09	17.75	14.01
SS-PCM-1.0	24.56	21.31	18.90	20.77
SS-PCM-2.0	25.61	34.74	16.92	32.85

T_m denotes the melting peak temperature, while T_c refers to the crystallization peak temperature.

3.1.3. Thermogravimetric Analysis (TGA)

Figure 7 presents the thermogravimetric (TG) and derivative thermogravimetric (DTG) curves of pure paraffin and SS-PCM particles. Most of the mass loss of pure paraffin occurred within a relatively narrow temperature range, beginning noticeably at around 120 °C and reaching its highest loss rate near 150 °C. Above 200 °C, the TG curve gradually leveled off, indicating that most of the paraffin volatilization and thermal decomposition had already occurred. The TG and DTG curves of the SS-PCMs followed trends similar to those of pure paraffin, and the onset of the main mass-loss stage remained nearly unchanged. This suggests that adsorption by the volcanic rock had little effect on the original thermal mass-loss behavior of paraffin. The limited change is mainly related to the physical adsorption and pore-confinement effects between paraffin and the volcanic rock, which only slightly affect the thermal decomposition characteristics of paraffin.

TGA results revealed differences in the high-temperature residual mass of SS-PCMs with different particle sizes, indicating variations in paraffin loading. The 2.0 mm SS-PCM showed the lowest residual mass, suggesting a relatively higher paraffin content. This observation agrees well with the DSC results, in which the same particle size exhibited a higher phase-change latent heat. In addition, the experimental temperature range in this study was −25–75 °C, with the upper limit well below the onset temperature of the main thermal mass-loss process of paraffin (approximately 120 °C). This indicates that the prepared SS-PCM does not undergo thermal decomposition within the experimental temperature range and can therefore satisfy the thermal stability requirements under the test conditions.

Based on the melting enthalpy of pure paraffin, the effective paraffin contents of the three SS-PCM groups were calculated from the DSC results to be approximately 8.5%, 12.8%, and 20.9%, respectively, whereas the corresponding mass loss percentages determined by thermogravimetric (TG) analysis were 13.3%, 21.2%, and 31.5%, resulting in differences of 4.8, 8.4, and 10.6 percentage points, respectively. Considering the high thermal stability of volcanic rock as an inorganic porous support, its mass was assumed to remain approximately stable over the investigated TG temperature range, and the loaded paraffin was completely volatilized or thermally decomposed during the test. Using the TG mass loss percentage as an approximation of the paraffin mass fraction in SS-PCM, the ratios of the effective paraffin content determined by DSC to the paraffin content estimated from TG analysis were calculated to be 63.9%, 60.4%, and 66.3%, respectively. The results indicate that both measurements exhibit an increasing trend with increasing paraffin loading. However, the effective phase-changing paraffin content estimated from DSC is lower than the paraffin content estimated from TG analysis. This discrepancy may be attributed to the confinement effect of volcanic rock pores on paraffin crystallization, interfacial interactions, and local heterogeneity in paraffin loading within the samples.

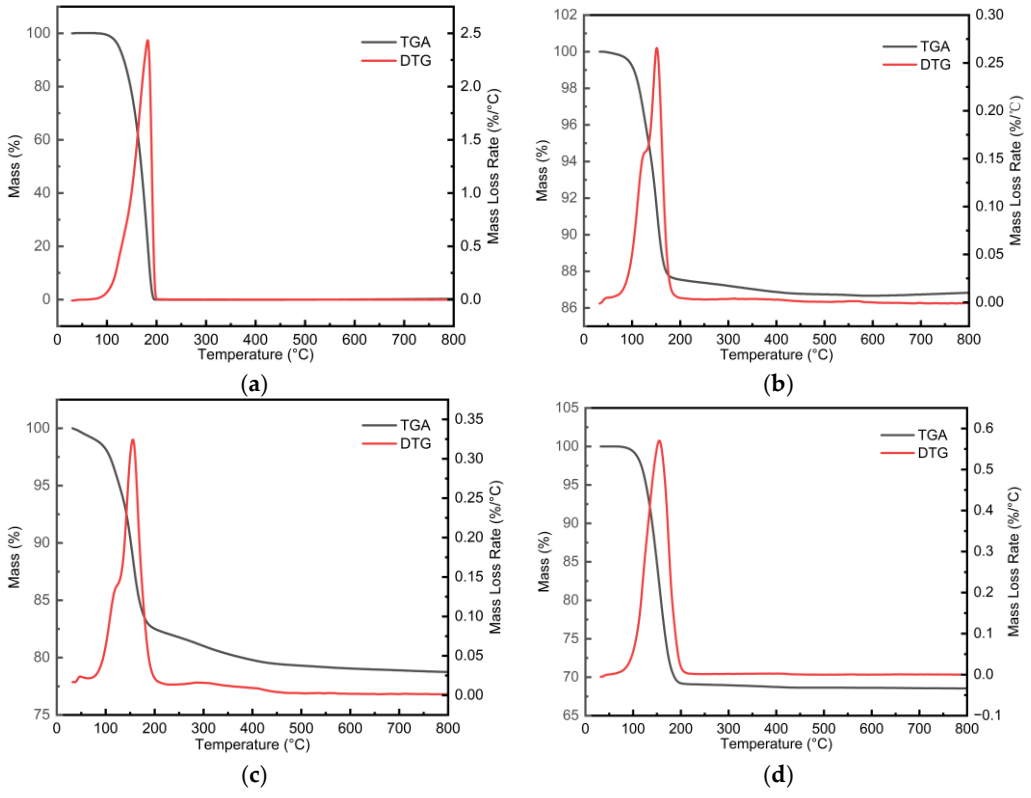


Figure 7. Thermogravimetric analysis (TGA) curves: (**a**) paraffin; (**b**) 0.5 mm SS-PCM; (**c**) 1.0 mm SS-PCM; and (**d**) 2.0 mm SS-PCM.

3.2. Thermal Energy Storage Performance Test

Figure 8 presents the temperature response curves of foam concrete specimens incorporating SS-PCM particles of different sizes during the heat storage and release processes. During the experiment, the bottom surface of each specimen was placed directly on a constant-temperature heating plate set at 50 °C. Heat was transferred upward through the specimen by one-sided heating from the bottom, while temperature variations were continuously monitored using a thermocouple positioned on the top surface of the specimen, with a data acquisition interval of 1 min. After 90 min of continuous heating, the heating plate was switched off, and the specimens were allowed to cool naturally in a constant-temperature environment of 15 °C. Temperature data were continuously recorded until 250 min to characterize the thermal response of foam concrete incorporating SS-PCM particles of different sizes during the heat storage and release processes.

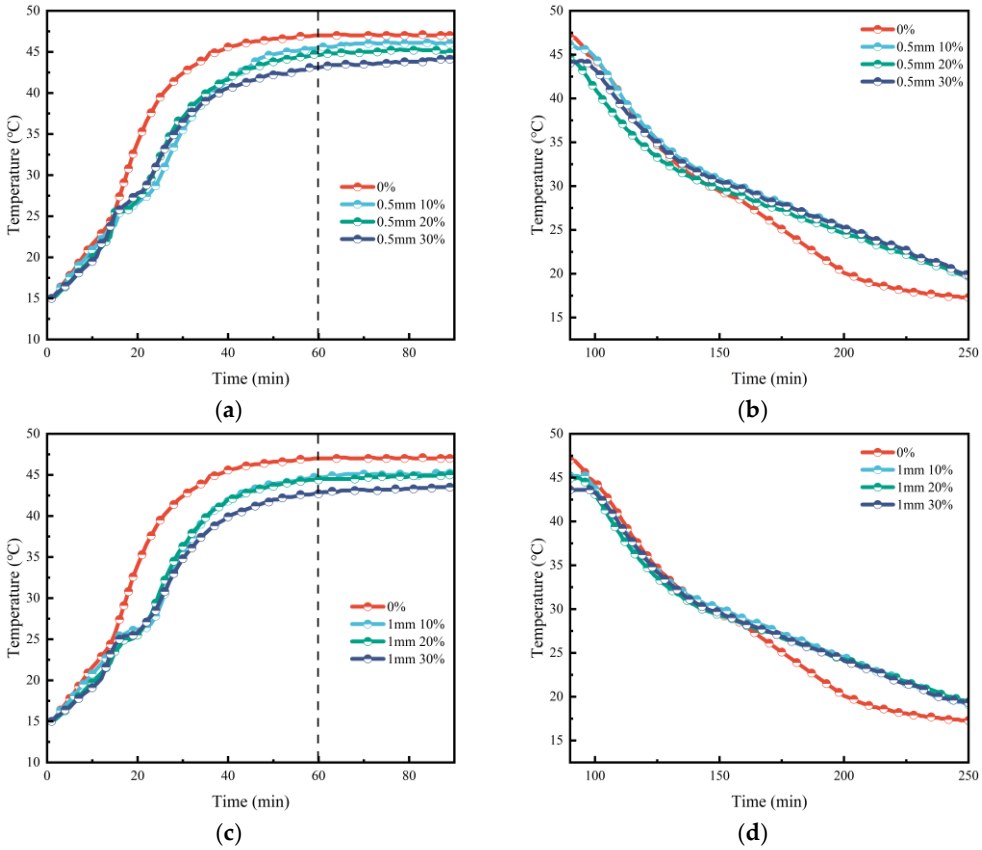
Figure 8 shows that the incorporation of SS-PCM noticeably slowed the temperature rise at the top surface of the foamed concrete specimens, and the temperature-regulation performance was jointly influenced by the SS-PCM particle size and volume fraction. After 60 min of heating, the top-surface temperature of the reference specimen without SS-PCM reached 47.0 °C, whereas all specimens containing SS-PCM exhibited lower top-surface temperatures. For the 0.5 mm SS-PCM group, increasing the volume fraction from 10% to 20% and 30% reduced the top-surface temperature to 45.5, 44.0, and 43.1 °C, with a maximum reduction of 8.3%. For the specimens containing 1.0 mm SS-PCM, the corresponding temperatures were 44.7, 44.4, and 42.7 °C, with a maximum reduction of 9.1%. By contrast, the specimens containing 2.0 mm SS-PCM exhibited a relatively smaller temperature decrease, with top-surface temperatures of 45.7, 45.5, and 45.4 °C at the three volume fractions and a maximum reduction of 3.4%. Overall, at a given SS-PCM particle size, the top-surface temperature of the specimens decreased with increasing SS-PCM volume fraction.

Although the 2.0 mm SS-PCM particles exhibit higher latent heat per unit mass, this advantage in thermal energy storage capacity does not necessarily translate into improved macroscopic temperature regulation performance of the foamed concrete specimens. This may be attributed to changes in interfacial heat transfer and internal heat transfer characteristics associated with increasing particle size. At the same volumetric incorporation level, an increase in SS-PCM particle size reduces the number of particles per unit volume and consequently decreases the total interfacial contact area between the particles and the cementitious matrix, thereby reducing the available heat exchange area between the matrix and the phase change material. Meanwhile, larger particles have relatively longer internal heat conduction paths, requiring more time for heat to transfer from the particle surface to the paraffin within the pores. This may increase the thermal response lag during the phase transition process, thereby limiting the effective utilization of latent heat within a limited temperature variation cycle. Furthermore, the pore connectivity and capillary forces within the volcanic rock facilitate paraffin impregnation and retention. However, differences in pore network structure and paraffin distribution among particles of different sizes may affect the extent to which the phase change material effectively participates in the phase transition process. Previous studies have demonstrated that the thermal response of phase change materials embedded in porous supports depends not only on their latent heat storage capacity but also on the pore structure, interfacial thermal resistance, and heat transfer pathways [34–36]. The temperature variation at the top surface of the specimen therefore reflects the overall thermal response resulting from the combined effects of the phase change material and the composite matrix.

During the cooling stage, the temperatures of all specimens gradually decreased after the heat source was switched off. However, the specimens incorporating SS-PCM exhibited a relatively slower cooling process, indicating that the incorporation of SS-PCM

altered the cooling rate and temperature response characteristics of foam concrete. This phenomenon may be attributed to changes in the thermophysical properties and internal heat transfer processes of the composite induced by the incorporation of SS-PCM particles. As the volumetric incorporation ratio of SS-PCM increased, changes in the material composition and heat transfer characteristics of the specimens influenced their cooling behavior to varying degrees. Considering both the heating and cooling stages, the incorporation of SS-PCM altered the temperature response behavior of foam concrete under heating and cooling conditions, demonstrating a certain degree of temperature regulation capability.

The constant-temperature heating plate test employed in this study was primarily designed to evaluate the relative temperature response performance of foam concrete specimens incorporating SS-PCM with different volumetric incorporation ratios and particle sizes under identical one-sided heating conditions. Due to the potential thermal contact resistance between the specimens and the heating plate, as well as the inevitable convective and radiative heat exchange between the specimen surfaces and the surrounding environment, the actual heat transfer process may be affected by heat losses and nonuniform internal temperature distributions. Furthermore, actual building envelopes are subjected to the combined effects of solar radiation, indoor–outdoor temperature differences, and dynamic ambient temperature variations, resulting in more complex thermal boundary conditions than those associated with the constant-temperature heating method employed in this study. Therefore, the results of this study primarily reflect the relative temperature regulation performance of the material during a single heat storage–release cycle under laboratory conditions and are insufficient to evaluate the long-term thermal stability of SS-PCM under repeated melting–solidification cycles.



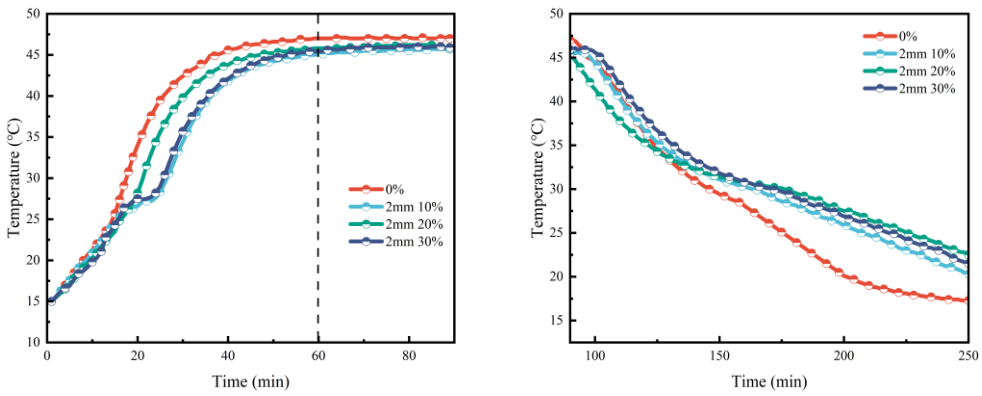


Figure 8. Temperature-response test results of specimens containing SS-PCM: (**a**,**b**) 0.5 mm; (**c**,**d**) 1.0 mm; and (**e**,**f**) 2.0 mm.

3.3. Compressive Strength

Figures 9 and 10 present the load–displacement curves and compressive strength results, respectively. Table 6 presents the mean compressive strength values of the specimens of SS-PCM foam concrete specimens under different testing temperatures, SS-PCM incorporation ratios, and particle sizes. Overall, both the peak load and compressive strength of the specimens exhibited decreasing trends with increasing testing temperature, indicating that elevated temperatures adversely affect the load-bearing capacity of foam concrete. Following the incorporation of SS-PCM, the compressive strength of the foam concrete specimens decreased to varying degrees. Under the combined effects of ambient temperature, SS-PCM incorporation ratio, and particle size, the compressive strength decreased by 4.2–43.0% compared with that of the corresponding specimens without SS-PCM. Among all specimens, the 10 vol% SS-PCM (1.0)/FC−25 specimen exhibited the smallest reduction in compressive strength, with a decrease of 0.59 MPa (4.2%) compared with the reference specimen without SS-PCM at the same temperature. In contrast, the 30 vol% SS-PCM (1.0)/FC-75 specimen exhibited the greatest reduction in compressive strength, decreasing by 4.43 MPa (43.0%) compared with the corresponding reference specimen at the same temperature.

As shown in Figure 10, under the same temperature and particle size conditions, the compressive strength of the foam concrete specimens generally decreased with increasing SS-PCM incorporation ratio, except for the specimens containing 30% SS-PCM at 75 °C in Figure 10a, which exhibited a slightly higher compressive strength than those containing 20% SS-PCM. Based on a comparison of the compressive strength values presented in Table 6, at the same temperature and SS-PCM incorporation ratio, foam concrete specimens incorporating 2.0 mm SS-PCM particles generally exhibited higher compressive strength than those incorporating 0.5 and 1.0 mm particles. The only exception was observed at −25 °C with an SS-PCM incorporation ratio of 10%, where the compressive strength of specimens containing 1.0 mm particles was slightly higher than that of specimens containing 2.0 mm particles. This behavior is likely related to the disruption of the cementitious load-bearing framework by SS-PCM particles, together with a reduction in stress transfer across the particle–matrix interface. As the SS-PCM volume fraction increased, the proportion of composite particles within the matrix also increased. This weakened the load-bearing capacity of the cement matrix and increased the number of vulnerable particle–matrix interfaces within the foamed concrete [37–39]. Therefore, the compressive strength of the foamed concrete specimens decreased with increasing SS-PCM volume fraction. At the same volume fraction, however, the 2.0 mm SS-PCM group contained the smallest number of particles, resulting in a lower total interfacial area between the particles and

the cementitious matrix. This reduced, to some extent, the adverse effect of weak interfacial regions on the overall load-bearing capacity. Consequently, in most cases, the incorporation of 2.0 mm SS-PCM had the least detrimental effect on the compressive strength of the specimens.

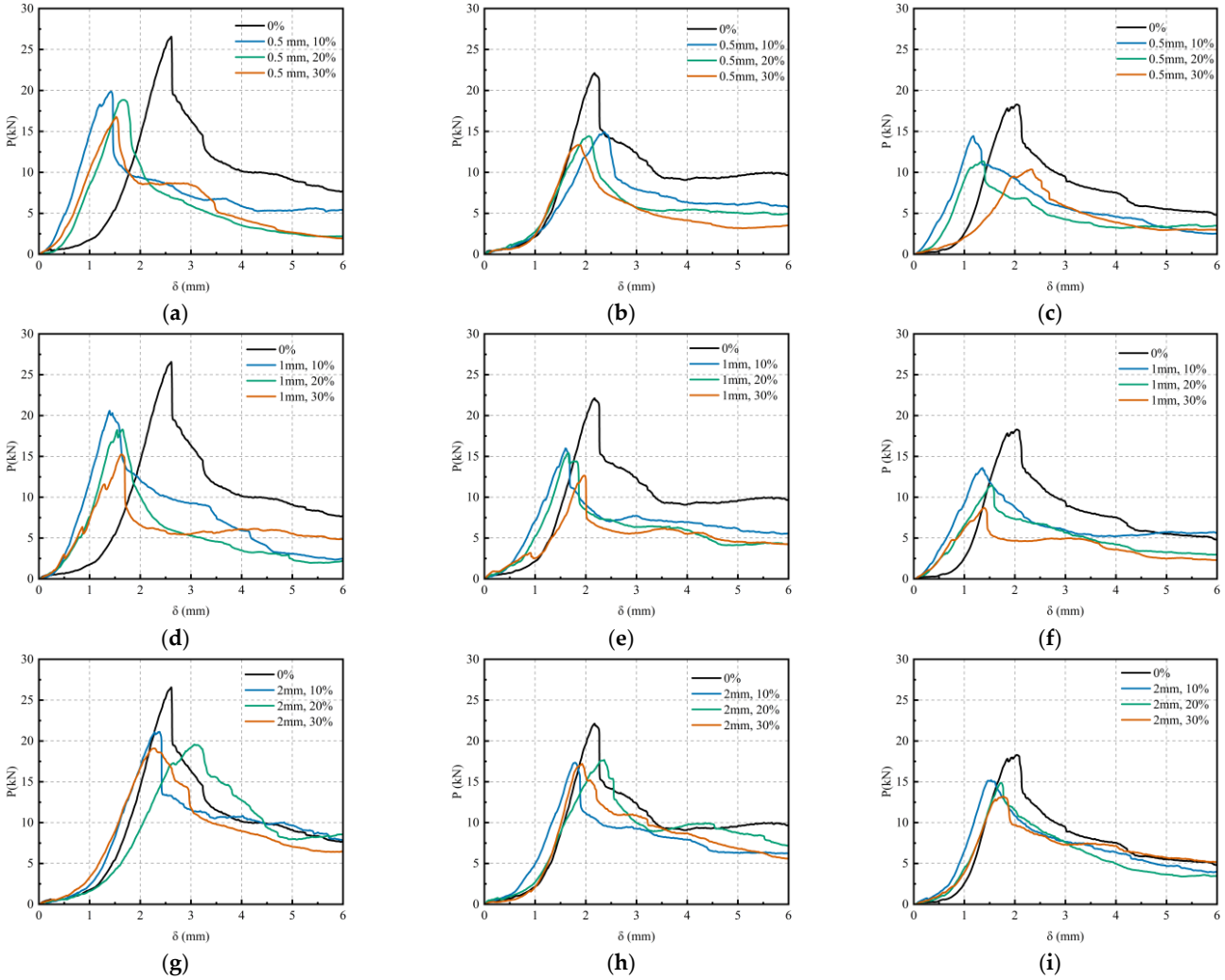
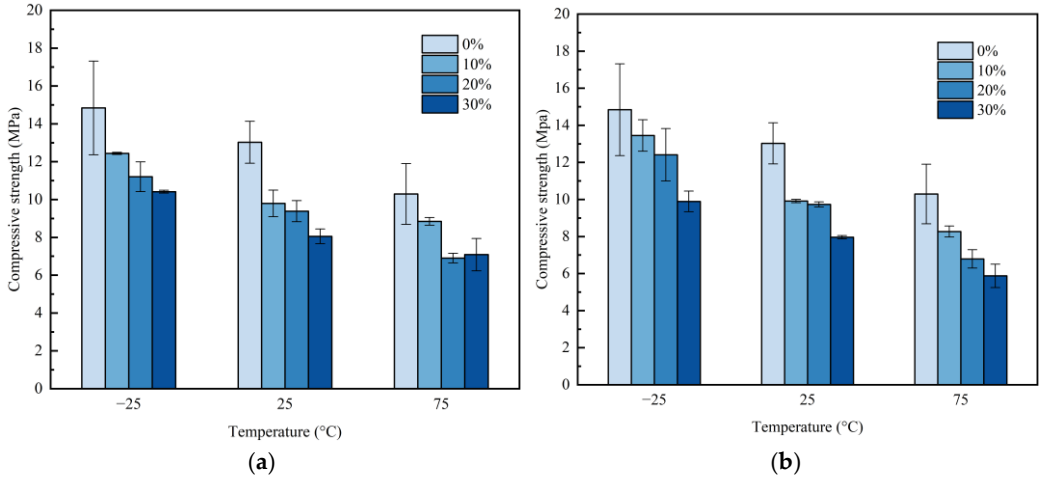


Figure 9. Load–displacement curves of the specimens at different temperatures: (**a**,**d**,**g**) −25 °C (**b**,**e**,**h**) 25 °C (**c**,**f**,**i**) 75 °C.



https://doi.org/10.3390/polym18232982

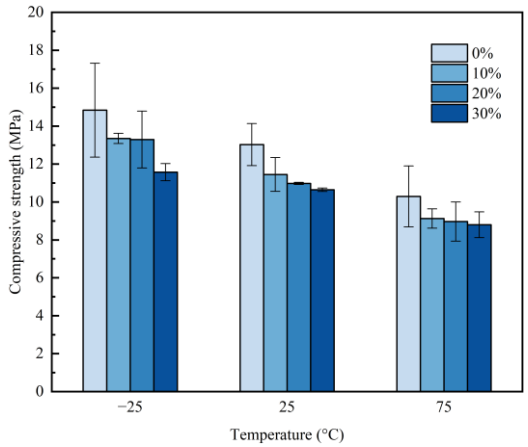


Figure 10. Compressive strength of specimens containing SS-PCM with different particle sizes: (**a**) 0.5 mm; (**b**) 1.0 mm; and (**c**) 2.0 mm. Error bars indicate the standard deviation of three independent measurements (n = 3).

Table 6. Mean compressive strength values of foam concrete specimens.

Group	Mean Compressive Strength (MPa)		
	−25 °C	**25 °C**	**75 °C**
0%	14.04	13.03	10.30
0.5 mm 10 vol%	12.44	9.80	8.85
0.5 mm 20 vol%	11.21	9.39	6.90
0.5 mm 30 vol%	10.42	8.06	7.09
1 mm 10 vol%	13.45	9.92	8.27
1 mm 20 vol%	12.41	9.74	6.79
1 mm 30 vol%	9.89	7.96	5.87
2 mm 10 vol%	13.35	11.45	9.13
2 mm 20 vol%	13.29	10.98	8.97
2 mm 30 vol%	11.57	10.65	8.80

3.4. Energy Absorption Performance Under Uniaxial Compression

Foamed concrete has a typical porous cellular structure and generally undergoes progressive damage processes, including pore collapse, cell-wall fracture, crack propagation, and structural densification under compressive loading, thereby exhibiting favorable energy absorption and dissipation capacity [40]. The presence of SS-PCM modified the pore structure and the particle–matrix interface, while also changing the compressive deformation response of the foamed concrete. Together, these effects altered the load-transfer mechanism and energy absorption during compression. The absorbed energy (E_a) was used to quantify the energy-absorption performance of volcanic rock–paraffin SS-PCM foamed concrete. The influence of ambient temperature, SS-PCM content, and particle size on the energy-absorption response of the specimens was examined [41,42].

The energy absorption (E_a) of each specimen was obtained from the area under the load–displacement curve, as given in Equation (3). Considering the differences in peak displacement and post-peak softening behavior of foam concrete specimens at different ambient temperatures, the reference specimens without SS-PCM (0% group) at each temperature were used as the basis for comparison to ensure the comparability of energy absorption performance among specimens tested at the same temperature. The displacement corresponding to a reduction in the post-peak load to 50% of the peak load was defined as the characteristic displacement (δ_{50}) for each temperature, which was then used as the common upper integration limit for all specimens tested at the corresponding

temperature. The energy absorption of each specimen was determined by calculating the area under the load–displacement curve over the displacement range from 0 to δ_{50}.

$$E_a = \int_0^{\delta} F(x)dx \quad (3)$$

Since the characteristic displacement (δ_{50}) varies with ambient temperature, the energy absorption calculated using this method was primarily used to evaluate the effects of SS-PCM particle size and volumetric incorporation ratio on the energy absorption performance of specimens tested at the same temperature. The calculated energy absorption values for all specimen groups are presented in Table 7. Overall, under the same temperature conditions, both SS-PCM particle size and volumetric incorporation ratio influenced the energy absorption capacity of the foam concrete specimens. Taking 75 °C as an example, when the volumetric incorporation ratio increased from 10% to 30%, the energy absorption of the specimens incorporating 0.5, 1.0, and 2.0 mm SS-PCM particles decreased by 37.0%, 37.6%, and 15.2%, respectively, indicating that the 2.0 mm group was relatively less sensitive to increases in the incorporation ratio. Regarding the effect of particle size, at both 25 °C and 75 °C, the specimens incorporating 2.0 mm SS-PCM particles exhibited higher energy absorption capacities than those incorporating 0.5 and 1.0 mm particles at all volumetric incorporation ratios. At a volumetric incorporation ratio of 30%, the energy absorption of the 2.0 mm group at 75 °C was 19.6 J, which was 44.1% higher than that of the 1.0 mm group. This trend is broadly consistent with the aforementioned compressive strength results, suggesting that the incorporation of larger SS-PCM particles may help mitigate the reduction in energy absorption capacity at high incorporation ratios, particularly at 25 °C and 75 °C.

The observed phenomena may be attributed to the effects of SS-PCM particle size on the continuity of the load-bearing framework of the cementitious matrix, the particle–matrix interfacial characteristics, and the damage evolution process under compressive loading. At the same volumetric incorporation ratio, larger SS-PCM particles result in a relatively smaller number of particles and a lower total interfacial area, which may, to some extent, mitigate the adverse effects of weak interfacial regions on the overall load-bearing capacity of the specimens. Consequently, the specimens may maintain higher load levels during compressive deformation, thereby exhibiting greater energy absorption capacity.

Table 7. Energy absorption values of specimens at three temperatures.

Group	E_a/J		
	−25 °C	**25 °C**	**75 °C**
0 vol% PCM/FC	30.4	28.4	24.1
10 vol% PCM (0.5 mm)/FC	29.2	20.4	23.0
20 vol% PCM (0.5 mm)/FC	25.4	19.6	17.3
30 vol% PCM (0.5 mm)/FC	26.4	18.4	14.5
10 vol% PCM (1 mm)/FC	31.9	22.9	21.8
20 vol% PCM (1 mm)/FC	24.4	20.9	17.9
30 vol% PCM (1 mm)/FC	20.3	16.1	13.6
10 vol% PCM (2 mm)/FC	27.5	24.9	23.1
20 vol% PCM (2 mm)/FC	24.2	25.9	20.9
30 vol% PCM (2 mm)/FC	29.5	24.9	19.6

3.5. Damage Analysis

To investigate the damage evolution behavior of foam concrete incorporating SS-PCM under different temperature conditions, a comparative analysis was conducted on specimens with different SS-PCM volumetric incorporation ratios (10%, 20%, and 30%) and particle sizes (0.5, 1.0, and 2.0 mm). The results indicate that all specimen groups exhibited similar temperature-dependent behavior and damage evolution patterns, although certain differences in the extent of damage were observed. Among them, the specimens with a volumetric incorporation ratio of 20% and a particle size of 1.0 mm exhibited more pronounced damage evolution characteristics. To highlight the influence of temperature on the damage behavior of the material and avoid repetitive discussion, this group was selected as a representative case for detailed analysis.

Figure 11 shows the load–displacement curves of 20 vol% PCM (1.0 mm)/FC at three temperatures, from which six characteristic points (A–F) were selected. The surface strain-field distributions corresponding to each characteristic point were obtained using the digital image correlation (DIC) method. Figure 12 compares the formation, propagation, and coalescence of surface strain-localization zones at different temperatures to elucidate the effects of temperature on crack initiation and ultimate failure modes in foamed concrete.

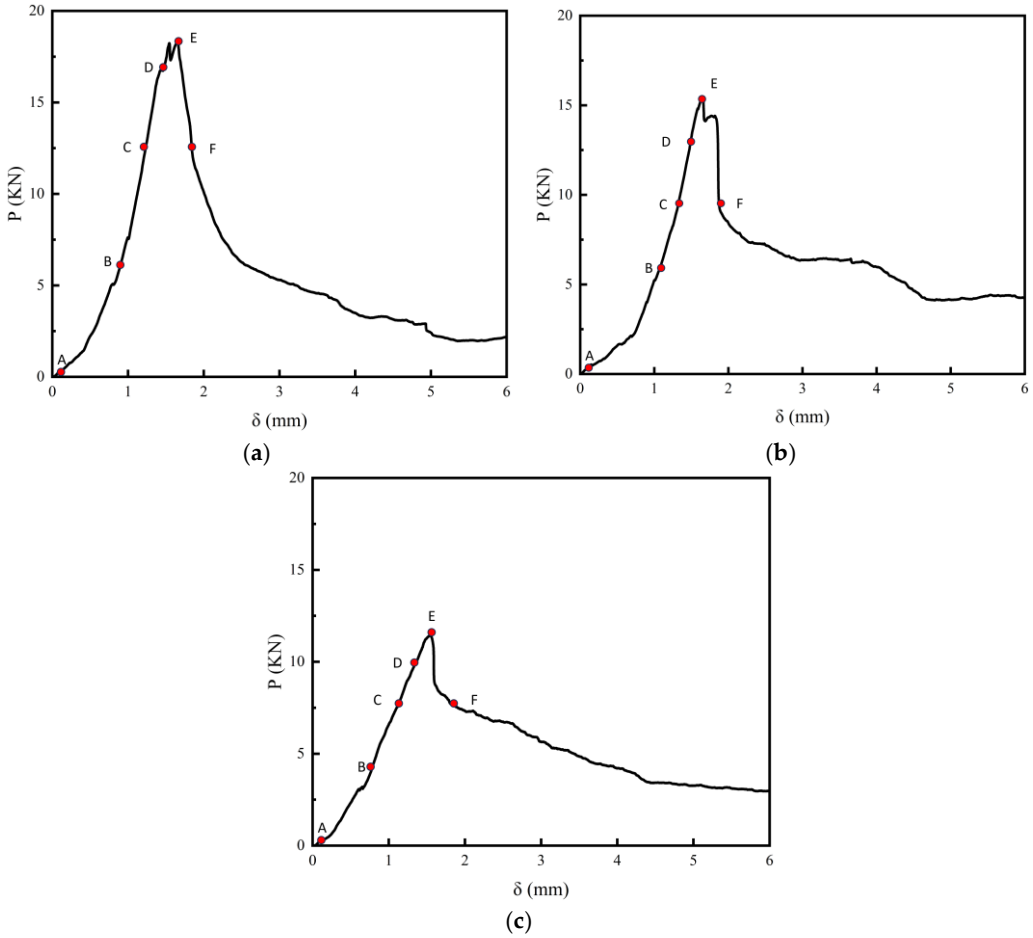
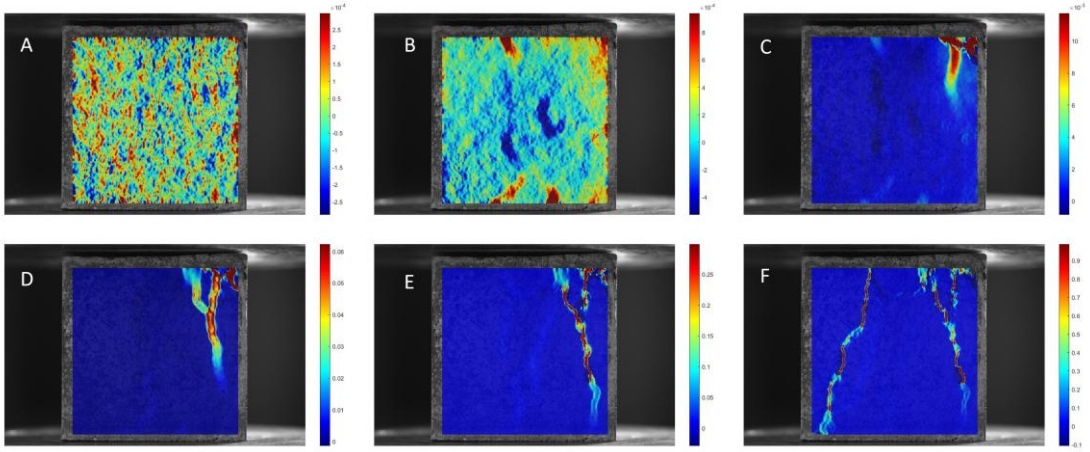


Figure 11. Load–displacement curves of SS-PCM specimens: (**a**) −25 °C; (**b**) 25 °C; and (**c**) 75 °C.

Based on the DIC analysis of the strain-field evolution corresponding to characteristic points A–F, the damage evolution process of the specimens was divided into two stages: the pre-peak stage and the post-peak stage. Pre-peak stage (A–E). Under all temperature conditions, the strain field of the specimens gradually evolved from an initially nonuniform distribution toward localized concentration. However, the specimens differed noticeably in where strain localization began and how it propagated afterward. At −25 °C,

the strain field was relatively diffuse at the early stage of loading. As the load increased, high-strain regions became concentrated near the upper-right part of the specimen and extended downward along the right side, eventually forming a predominantly longitudinal localization band on one side. At 25 °C, high-strain regions first appeared near the top of the specimen. As loading continued, several localization paths developed downward from different initiation points, giving rise to a more dispersed propagation pattern. At 75 °C, several strain-concentration zones appeared in the upper part of the specimen. With continued loading, the localization bands extended obliquely inward from different positions and gradually converged near the center, eventually forming an approximately Y-shaped strain-localization pattern. Overall, increasing the ambient temperature noticeably changed the pre-peak damage pattern. At lower temperatures, damage developed mainly along a relatively concentrated path, whereas at higher temperatures, several paths formed simultaneously and gradually converged.

Post-peak stage (E–F). After the specimens reached the peak load, the existing strain-localization bands continued to develop, and the accumulated damage progressively evolved into macroscopic failure. At −25 °C, the right-side strain localization band extended downward, accompanied by the formation of a new high-strain path on the left side of the specimen. The final failure was marked by two longitudinal localization bands extending along both sides of the specimen. At 25 °C, the localization bands that appeared before the peak load intensified and extended downward. As loading continued, these bands gradually merged into two inclined through-going paths, giving rise to a multipath failure pattern. At 75 °C, the Y-shaped localization structure formed before the peak load developed further, with high-strain bands continuing to propagate along the existing paths and extending toward the lower part of the specimen, ultimately resulting in a failure mode characterized by multipath coalescence and through-going propagation. Overall, increasing ambient temperature altered the development paths of strain localization in the specimens, causing the failure mode to evolve from predominantly edge-oriented longitudinal propagation at low temperature to a more complex pattern characterized by multipath propagation, coalescence, and through-going failure at high temperature.



(**a**)

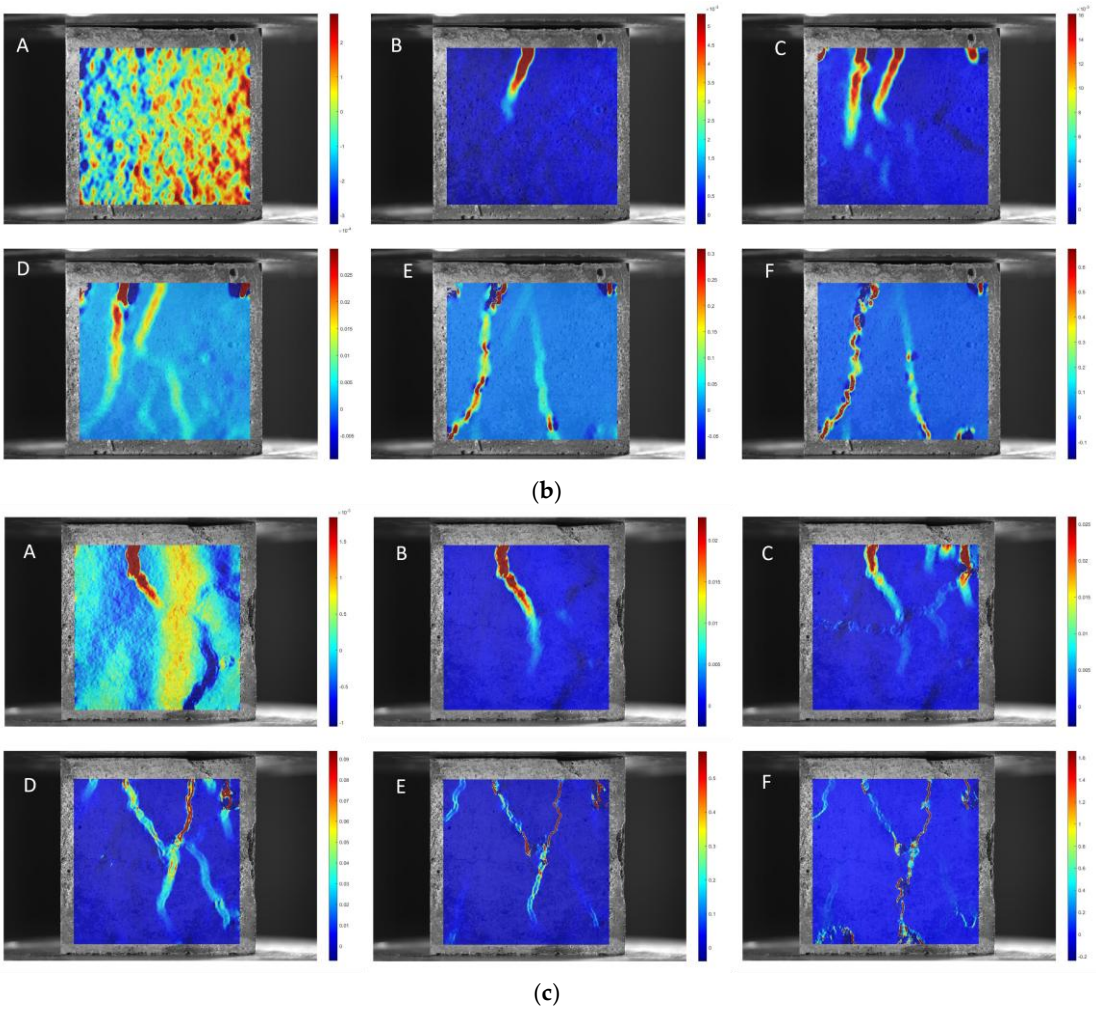


Figure 12. Horizontal strain contour maps of the specimens at different loading stages under different temperatures: (**a**) −25 °C; (**b**) 25 °C; and (**c**) 75 °C.

4. Conclusions

In this study, porous volcanic rock was used as the supporting matrix and paraffin as the phase change component to prepare a volcanic rock–paraffin shape-stabilized phase change material (SS-PCM) by vacuum adsorption, which was subsequently incorporated into foamed concrete. Temperature-response tests, uniaxial compression tests, and digital image correlation (DIC) were employed to systematically investigate the effects of SS-PCM particle size, volume fraction, and ambient temperature on the heat-storage and heat-release performance, compressive behavior, energy-absorption characteristics, and damage evolution of foamed concrete. The variations in the thermal and mechanical properties of the material under different parameter combinations were elucidated. The main findings are summarized below:

(1) The paraffin-based SS-PCM prepared by vacuum adsorption exhibited good thermal stability and excellent thermal energy-storage performance. Variations in particle size had only a limited effect on the phase-change temperature of the SS-PCM, with a maximum deviation of only 1.49 °C from that of pure paraffin. Furthermore, the DSC and TGA results showed that the 2.0 mm SS-PCM exhibited superior latent heat storage performance compared with the 0.5 and 1.0 mm SS-PCMs.

(2) The incorporation of SS-PCM improved the temperature regulation performance of foam concrete, with the effectiveness of temperature regulation being influenced by both particle size and volumetric incorporation ratio. After 60 min of heating, the

maximum reductions in the top surface temperature of specimens incorporating SS-PCM particles with sizes of 0.5, 1.0, and 2.0 mm were 3.9, 4.3, and 1.6 °C, respectively, compared with the control group without SS-PCM, corresponding to temperature reductions of 8.3%, 9.1%, and 3.4%, respectively. Among them, the 1.0 mm SS-PCM exhibited the best temperature regulation performance, whereas the 2.0 mm SS-PCM showed a relatively weaker temperature regulation effect. Although the 2.0 mm SS-PCM exhibited a higher latent heat storage capacity, its temperature regulation performance at the foam concrete specimen scale did not improve correspondingly, indicating that the latent heat storage capacity of SS-PCM is not the sole factor determining the thermal response performance of the composite material.

(3) Increasing ambient temperature and SS-PCM volumetric incorporation ratio generally reduced the compressive strength of foam concrete. At ambient temperatures of −25, 25, and 75 °C, the incorporation of SS-PCM resulted in compressive strength reductions ranging from 4.2% to 43.0% compared with the corresponding control specimens without SS-PCM at the same temperature. At −25 °C, the compressive strength of specimens incorporating 10 vol% SS-PCM with a particle size of 1.0 mm decreased by only 0.59 MPa, corresponding to a strength reduction of 4.2%. In contrast, at 75 °C, increasing the volumetric incorporation ratio of 1.0 mm SS-PCM to 30 vol% resulted in a compressive strength reduction of 4.43 MPa, corresponding to a strength loss of 43.0%. Overall, the incorporation of SS-PCM at lower volumetric incorporation ratios had a relatively minor effect on the compressive strength of foam concrete, whereas more pronounced strength reductions were observed under high-temperature conditions and at higher incorporation ratios.

(4) DIC analysis revealed clear differences in the damage evolution and final failure pattern of SS-PCM foamed concrete at different ambient temperatures. With increasing ambient temperature, the foamed concrete no longer failed along a single dominant path. Instead, multiple cracks developed, branched, and gradually connected to form through-going failure paths.

Author Contributions: Conceptualization, H.Y.; methodology, H.Y.; software, C.L. and R.M., validation, C.L.; formal analysis, H.Y.; resources, R.M.; data curation, R.M.; writing—original draft preparation, C.L.; writing—review and editing, H.Y.; visualization, C.L. and R.M.; supervision, H.Y.; funding acquisition, H.Y. All authors have read and agreed to the published version of the manuscript.

Funding: The authors would like to thank the financial support from the Natural Science Foundation of Ningxia (Project No. 2026AAC030347), the Young and Middle-aged Key Personnel Project of North Minzu University (Project No. 2025BG265), and the Graduate Innovation Project of North Minzu University (Project No. YCX26263).

Institutional Review Board Statement: Not applicable.

Data Availability Statement: The original contributions presented in this study are included in the article. Further inquiries can be directed to the corresponding author.

Conflicts of Interest: The authors declare no conflicts of interest.

Abbreviations

The following abbreviations are used in this manuscript:

SS-PCM	Shape-stabilized phase change material
FC	Foam concrete
DIC	Digital Image correlation

References

1. Faraj, K.; Khaled, M.; Faraj, J.; Hachem, F.; Castelain, C. Phase change material thermal energy storage systems for cooling applications in buildings: A review. *Renew. Sustain. Energy Rev.* **2020**, *119*, 109579. https://doi.org/10.1016/j.rser.2019.109579.
2. Ben Romdhane, S.; Amamou, A.; Ben Khalifa, R.; Said, N.M.; Younsi, Z.; Jemni, A. A review on thermal energy storage using phase change materials in passive building applications. *J. Build. Eng.* **2020**, *32*, 101563. https://doi.org/10.1016/j.jobe.2020.101563.
3. Sharshir, S.W.; Joseph, A.; Elsharkawy, M.; Hamada, M.A.; Kandeal, A.; Elkadeem, M.R.; Thakur, A.K.; Ma, Y.; Moustapha, M.E.; Rashad, M.; et al. Thermal energy storage using phase change materials in building applications: A review of the recent development. *Energy Build.* **2023**, *285*, 112908. https://doi.org/10.1016/j.enbuild.2023.112908.
4. Jha, S.K.; Sankar, A.; Zhou, Y.; Ghosh, A. Incorporation of phase change materials in buildings. *Constr. Mater.* **2024**, *4*, 676–703. https://doi.org/10.3390/constrmater4040037.
5. Pereira, J.; Souza, R.; Oliveira, J.; Moita, A. Phase change materials in residential buildings: Challenges, opportunities, and performance. *Materials* **2025**, *18*, 2063. https://doi.org/10.3390/ma18092063.
6. Masood, U.; Haggag, M.; Hassan, A.; Laghari, M. A review of phase change materials as a heat storage medium for cooling applications in the built environment. *Buildings* **2023**, *13*, 1595. https://doi.org/10.3390/buildings13071595.
7. Jeon, I.K.; Abdullah, A.; Al Jebaei, H.; Kim, Y.R.; Aryal, A.; Baltazar, J.C. Effects of shape-stabilized phase change materials in cementitious composites on thermal-mechanical properties and economic benefits. *Appl. Therm. Eng.* **2023**, *219*, 119444. https://doi.org/10.1016/j.applthermaleng.2022.119444.
8. Alkhazaleh, A.H.; Almanaseer, W.; Ismail, M.; Almashaqbeh, S.; Farid, M.M. Thermal and mechanical properties of cement based-composite phase change material of butyl stearate/isopropyl palmitate/expanded graphite for low temperature solar thermal applications. *J. Energy Storage* **2022**, *50*, 104547. https://doi.org/10.1016/j.est.2022.104547.
9. Zhou, D.; Xiao, S.; Liu, Y. Preparation and characterization of innovative cement mortar incorporating fatty acid/expanded graphite composite phase change material for thermal energy storage. *Sci. Rep.* **2024**, *14*, 16523. https://doi.org/10.1038/s41598-024-67573-x.
10. Štukovnik, P.; Bokan-Bosiljkov, V.; Marinšek, M.; Skalar, T. Cement composites with the addition of phase-change materials as innovative construction materials for maintaining a pleasant living environment. *Mater. Technol.* **2024**, *58*, 379–386. https://doi.org/10.17222/mit.2023.997.
11. Beskopylny, A.N.; Stel'makh, S.A.; Shcherban', E.M.; Shakhalieva, D.M.; Chernil'nik, A.; Panfilov, I.; Beskopylny, N.; Özkılıç, Y.O. Finite element modeling and experimental study of foam concrete and polystyrene concrete. *Buildings* **2026**, *16*, 737. https://doi.org/10.3390/buildings16040737.
12. Yildizel, S.A.; Özkılıç, Y.O.; Yavuz, A. Optimization of waste tyre steel fiber and rubber added foam concretes using Taguchi method and artificial neural networks. *Structures* **2024**, *61*, 106098. https://doi.org/10.1016/j.istruc.2024.106098.
13. Mydin, M.A.O.; Awoyera, P.O.; Taqieddin, Z.N.; Özkılıç, Y.O.; Fadugba, O.G.; Abdullah, M.M.A.B.; Omar, R.; Datta, S.D.; Olalusi, O.B. Green construction with sustainable foam mortar utilizing recycled polyethylene terephthalate waste for enhanced thermal insulation and durability properties. *Sci. Rep.* **2025**, *15*, 33633. https://doi.org/10.1038/s41598-025-06141-3.
14. Hao, L.; Xiao, J.; Cao, W.; Sun, J. Experimental study and assessment of thermal energy storage mortar with paraffin/recycled brick powder composite phase change materials. *Front. Struct. Civ. Eng.* **2022**, *16*, 1301–1314. https://doi.org/10.1007/s11709-022-0883-4.
15. Zhang, B.; Yang, H.; Xu, T.; Tang, W.; Cui, H. Mechanical and thermo-physical performances of cement-based composites containing diatomite/paraffin phase change material. *Appl. Sci.* **2021**, *11*, 468. https://doi.org/10.3390/app11020468.
16. Yang, X.; Liu, Y.; Tian, W.; Niu, K.; Wei, Y. Experimental and numerical study of microencapsulated PCM effects on hydration and mechanical behaviour of alkali-activated slag-fly ash binders. *Constr. Build. Mater.* **2025**, *499*, 143973. https://doi.org/10.1016/j.conbuildmat.2025.143973.
17. Zheng, Y.; Zhang, J.; Xia, Z.; Huang, W.; Liu, S.; Zhang, R.; Wu, Q. Mechanical and thermal properties of phase change microencapsulated foam concrete. *Case Stud. Constr. Mater.* **2026**, *24*, e06072. https://doi.org/10.1016/j.cscm.2026.e06072.
18. Kocyigit, F.; Bayram, M.; Hekimoglu, G.; Cay, V.V.; Gencel, O.; Ustaoglu, A.; Sarı, A.; Erdogmus, E.; Ozbakkaloglu, T. Thermal energy saving and physico-mechanical properties of foam concrete incorporating form-stabilized basalt powder/capric acid based composite phase change material. *J. Clean. Prod.* **2023**, *414*, 137617. https://doi.org/10.1016/j.jclepro.2023.137617.
19. Fu, W.; Lao, J.; Zhou, W.; Chen, L.; Ma, J.; He, Z.; Tan, B.; Zhou, Q. Experimental and numerical investigations on phase change thermal storage foam concrete based on $CaCl_2 \cdot 6H_2O$/silica aerogel composite phase change material. *J. Energy Storage* **2024**, *103*, 114371. https://doi.org/10.1016/j.est.2024.114371.

20. Laafer, A.; Hammouma, T.; Hmida, A.; Bourouis, M. Comprehensive review of phase change materials for building applications: Passive, active, and hybrid systems (2022–2025). *Energies* **2026**, *19*, 1151. https://doi.org/10.3390/en19051151.
21. Gandhi, M.; Kumar, A.; Elangovan, R.; Meena, C.S.; Kulkarni, K.S.; Kumar, A.; Bhanot, G.; Kapoor, N.R. A review on shape-stabilized phase change materials for buildings. *Sustainability* **2020**, *12*, 9481. https://doi.org/10.3390/su12229481.
22. Zhu, N.; Li, S.; Hu, P.; Wei, S.; Deng, R.; Lei, F. A review on applications of shape-stabilized phase change materials embedded in building enclosure in recent ten years. *Sustain. Cities Soc.* **2018**, *43*, 251–264. https://doi.org/10.1016/j.scs.2018.08.028.
23. Yazdani McCord, R.; Baniasadi, H. Advancements in form-stabilized phase change materials: Stabilization mechanisms, multi-functionalities, and applications—A comprehensive review. *Mater. Today Energy* **2024**, *41*, 101532. https://doi.org/10.1016/j.mtener.2024.101532.
24. Mohaisen, K.O.; Zahir, M.H.; Maslehuddin, M.; Al-Dulaijan, S.U. Development of a shape-stabilized phase change material utilizing natural and industrial byproducts for thermal energy storage in buildings. *J. Energy Storage* **2022**, *50*, 104205. https://doi.org/10.1016/j.est.2022.104205.
25. Gouissem, L.; Rouabah, F. Preparation of a New Shape-Stable Phase-Change Material Based on Expanded Perlite, Paraffin, Epoxy, Copper and High-Density Polyethylene. *Sustain. Polym. Energy* **2024**, *2*, 10012. https://doi.org/10.70322/spe.2024.10012.
26. Przybek, A.; Hebdowska-Krupa, M.; Łach, M. Paraffin Coated with Diatomite as a Phase Change Material for Thermal Energy Storage. *Materials* **2025**, *18*, 5166. https://doi.org/10.3390/ma18225166.
27. Yu, Z.; Shao, R.; Li, J.; Wu, C. An In-Depth Review of Phase Change Materials in Concrete for Enhancing Building Energy-Efficient Temperature Control Systems. *J. Energy Storage* **2024**, *104*, 114533. https://doi.org/10.1016/j.est.2024.114533.
28. Sharma, R.; Jang, J.-G.; Hu, J.-W. Phase-Change Materials in Concrete: Opportunities and Challenges for Sustainable Construction and Building Materials. *Materials* **2022**, *15*, 335. https://doi.org/10.3390/ma15010335.
29. Rashid, F.L.; Al-Obaidi, M.A.; Dulaimi, A.; Bernardo, L.F.A.; Eleiwi, M.A.; Mahood, H.B.; Hashim, A. A Review of Recent Improvements, Developments, Effects, and Challenges on Using Phase-Change Materials in Concrete for Thermal Energy Storage and Release. *J. Compos. Sci.* **2023**, *7*, 352. https://doi.org/10.3390/jcs7090352.
30. Gencel, O.; Bilir, T.; Bademler, Z.; Ozbakkaloglu, T. A detailed review on foam concrete composites: Ingredients, properties, and microstructure. *Appl. Sci.* **2022**, *12*, 5752. https://doi.org/10.3390/app12115752.
31. He, B.; Martin, V.; Setterwall, F. Phase transition temperature ranges and storage density of paraffin wax phase change materials. *Energy* **2004**, *29*, 1785–1804. https://doi.org/10.1016/j.energy.2004.03.002.
32. Blaber, J.; Adair, B.; Antoniou, A. Ncorr: Open-Source 2D Digital Image Correlation Matlab Software. *Exp. Mech.* **2015**, *55*, 1105–1122. https://doi.org/10.1007/s11340-015-0009-1.
33. Li, H.; Liu, X. Enhanced Thermal Properties of Carbon-Based Composite Phase Change Materials Towards Energy Efficiency. *Materials* **2026**, *19*, 3960. https://doi.org/10.3390/ma19183960.
34. Zhang, Y.; Zheng, S.; Zhu, S.; Ma, J.; Sun, Z.; Farid, M. Evaluation of paraffin infiltrated in various porous silica matrices as shape-stabilized phase change materials for thermal energy storage. *Energy Convers. Manag.* **2018**, *171*, 361–370. https://doi.org/10.1016/j.enconman.2018.06.002.
35. Li, Y.; Dong, M.; Song, W.; Liang, X.; Chen, Y.; Liu, Y. Preparation and characterization of paraffin/mesoporous silica shape-stabilized phase change materials for building thermal insulation. *Materials* **2021**, *14*, 1775. https://doi.org/10.3390/ma14071775.
36. Zhang, S.; Feng, D.; Shi, L.; Wang, L.; Jin, Y.; Tian, L.; Li, Z.; Wang, G.; Zhao, L.; Yan, Y. A review of phase change heat transfer in shape-stabilized phase change materials (ss-PCMs) based on porous supports for thermal energy storage. *Renew. Sustain. Energy Rev.* **2021**, *135*, 110127. https://doi.org/10.1016/j.rser.2020.110127.
37. Vargas, P.; Restrepo-Baena, O.; Tobón, J.I. Microstructural analysis of interfacial transition zone (ITZ) and its impact on the compressive strength of lightweight concretes. *Constr. Build. Mater.* **2017**, *137*, 381–389. https://doi.org/10.1016/j.conbuildmat.2017.01.101.
38. Im, S.; Liu, J.; Cho, S.; Moon, J.; Park, J.; Wi, K.; Seok, S.; Lim, S.; Bae, S. Quantitative characterization of the interfacial transition zone around lightweight and normal aggregates in cement mortars at different water-to-binder ratios. *Constr. Build. Mater.* **2023**, *400*, 132584. https://doi.org/10.1016/j.conbuildmat.2023.132584.
39. Bentz, D.P. Influence of internal curing using lightweight aggregates on interfacial transition zone percolation and chloride ingress in mortars. *Cem. Concr. Compos.* **2009**, *31*, 285–289. https://doi.org/10.1016/j.cemconcomp.2009.03.001.
40. Feng, S.; Zhou, Y.; Li, Q.M. Damage behavior and energy absorption characteristics of foamed concrete under dynamic load. *Constr. Build. Mater.* **2022**, *357*, 129340. https://doi.org/10.1016/j.conbuildmat.2022.129340.

41. Zhang, J.; Lin, M.; Xiao, D.; Pu, C.; Liao, J.; Li, X. Influence of the porosity and pore size on the mechanical properties and energy dissipation of cellular concrete utilizing millimeter-size SAP. *Constr. Build. Mater.* **2024**, *417*, 135298. https://doi.org/10.1016/j.conbuildmat.2024.135298.
42. Lei, Z.; Liu, J.; Guo, Z.; Ye, J.; Gao, F.; Di, H.; Wang, Z. Metal honeycomb skeleton reinforced foam concrete: Mechanical properties, reinforcement mechanism and optimal design. *Eng. Struct.* **2025**, *341*, 120827. https://doi.org/10.1016/j.engstruct.2025.120827.

Disclaimer/Publisher's Note: The statements, opinions and data contained in all publications are solely those of the individual author(s) and contributor(s) and not of MDPI and/or the editor(s). MDPI and/or the editor(s) disclaim responsibility for any injury to people or property resulting from any ideas, methods, instructions or products referred to in the content.